Influence of group VIB metals on activity of the Ni/MgO catalysts for methane decomposition

Ali Rastegarpanah[a], Mehran Rezaei[b,*], Fereshteh Meshkani[a,c], Kunfeng Zhang[d], Xingtian Zhao[d], Wenbo Pei[d], Yuxi Liu[d], Jiguang Deng[d], Hamidreza Arandiyan[e], Hongxing Dai[d,**]

[a] Catalyst and Advanced Materials Research Laboratory, Chemical Engineering Department, Faculty of Engineering, University of Kashan, Kashan, Iran
[b] School of Chemical, Petroleum and Gas Engineering, Iran University of Science and Technology (IUST), Tehran, Iran
[c] Institute of Nanoscience and Nanotechnology, University of Kashan, Kashan, Iran
[d] Beijing Key Laboratory for Green Catalysis and Separation, Key Laboratory of Beijing on Regional Air Pollution Control, Laboratory of Catalysis Chemistry and Nanoscience, Department of Chemistry and Chemical Engineering, College of Environmental and Energy Engineering, Beijing University of Technology, Beijing 100124, China
[e] Laboratory of Advanced Catalysis for Sustainability, School of Chemistry, The University of Sydney, Sydney 2006, Australia

ARTICLE INFO

ABSTRACT

Mesoporous 55 wt.% Ni/MgO and group VIB metal (Cr, Mo or W)-doped catalysts were prepared using the facile "one-pot" evaporation-induced self-assembly in ethanol and wetness impregnation methods, respectively. Physicochemical properties of the as-prepared catalysts were characterized by means of the BET, XRD, SEM, TEM, HAADF, XPS, H_2-TPR, TPO, and Raman techniques. The doping of Cr to 55 wt% Ni/MgO improved catalytic activity and stability for the decomposition of methane under harsh reaction conditions. The maximal initial methane conversions of 80, 87, and 75% were achieved over the 55 wt.% $Ni-x$Cr/MgO (denoted as $55Ni-x$Cr/MgO; x = 5, 10, and 15 wt.%) at 675 °C and GHSV = 48,000 mL/(g h), respectively. It is concluded that the high catalytic efficiency of the Cr-doped sample in methane decomposition was associated with its high surface area, high oxygen adspecies concentration, and good low-temperature reducibility. In addition, multi-walled carbon filaments with metal-encapsulated carbon particles were deposited on the Cr-doped catalysts, and the ordered carbon filaments with different diameters and good crystallinity were produced on the surface of the $55Ni-10$Cr/MgO catalyst.

1. Introduction

In recent years, a steady increase of methane and carbon dioxide concentrations in the atmosphere has sparked interest of scientific community in discovering quick solutions to the greenhouse and global warming effects. Despite the fact that in the atmosphere methane concentration is lower than carbon dioxide, the former has remarkably led to the overall global warming up to 20% [1,2]. Conventionally, methane is produced from natural sources (such as termites, wildfires, and wetlands) and human activities (such as landfills, coal mining, and agricultural activities) [3]. As an example, landfill gas only consists of about 45% CH_4 and 65% CO_2, but methane production from landfill leads to about one-third of all the emitted methane in the USA. Methane is also a main component of natural gas, its release to the atmosphere can induce greenhouse effect [2,4]. Due to the demand for reducing the

substantial dependency on petroleum-based resources (98% of energy is produced from fossil fuels) and controlling the undesirable influence of methane on the atmosphere, new renewable alternative energies are immediately needed for substituting the current energy sources [5–8].

Hydrogen has played an important role in serving as an attractive renewable alternative energy in recent decades [9,10]. This is because hydrogen can produce energy (39.40 kW h/kg) three times more than the liquid hydrocarbons (13.10 kW h/kg) and can be converted into electricity and other energy forms without pollution [11]. In this regard, more concentrated research activities are conducted for the production of CO_x-free hydrogen with a high purity. Since H_2 has a high tendency to react with other components (e.g., C and O_2) and no pure H_2 is available in nature, it should be produced using other resources (e.g., natural gas) [12]. The H/C ratio (4) in methane is the highest among all of the hydrocarbons, and conversion of methane can produce

a larger amount of hydrogen than that of other hydrocarbons. Among the various methods for hydrogen production from methane, dry and steam reforming are the most economical and conventional technologies, which generate about 50% of the world hydrogen consumption [13]. The two pathways, however, produce hydrogen with carbon oxides (CO_x) that are harmful to the environmental and not favorable for the direct utilization of hydrogen in the low-temperature fuel cells since CO in a ppm level can poison the alkaline fuel cells [10,14]. Unlike the reforming process which produces a mixture of H_2 and CO_x, catalytic methane decomposition can generate CO_x-free hydrogen and solid carbon, which is highly desirable for the use in fuel cells. On the other hand, the mixture of CH_4 and H_2 is a more operative fuel for gas turbine power plants and internal combustion engines than oil or natural gas [15].

Catalytic decomposition of methane ($CH_4 \rightarrow C + 2H_2$; $\Delta H°_{293} = 74.80$ kJ/mol) is a mildly endothermic one-step reaction and interesting from a viewpoint of production of highly pure hydrogen and carbon nanofibers as a byproduct (they have a wide range of potential applications, such as polymer additives, electronic components, and catalyst supports [16]). In addition, this process is more energy efficient and environmentally benign than the dry or steam reforming of methane [17,18]. It was reported that the supported Ni particles were one of the promising catalysts for methane decomposition since Ni has the partially filled 3d orbitals that would lead to methane cracking quickly by the partial acceptance of electrons [19]. Magnesium oxide is used for supports, CO_2 adsorbents, and agents for waste water purification [20]. It has been reported that as compared with other metal oxides, MgO nanoparticles are excellent catalyst support because of their small particle sizes. When the particle size decreases, the number of surface atoms increases, and therefore the activity is expected to improve [21]. MgO have been already used as supported catalysts for different reactions, such as dry and steam reforming of CH_4, Fischer–Tropsch synthesis, water–gas shift, and other organic-involved reactions [22–25]. Previously, our group observed that the MgO-supported Ni catalysts showed an acceptable activity and better stability for methane decomposition in the range of 575−700 °C; at high temperatures, however, the supported Ni catalysts exhibited a dramatic decline in stability owing to the sintering of Ni particles and the covering of active sites by the deposited carbon [26]. This challenge can be improved by the doping of a second metal to the supported Ni catalyst. There have been several studies on the doping of metals (e.g., La, Co, Fe, Ce, Cu, Pd, Rh, Pd, Ir, and Pt) to the supported Ni catalysts in the literature [6,26–31]. For example, Takenaka et al. investigated the addition of Cu, Rh, Pd, Ir, and Pt to the supported Ni catalyst, and found that the doping of Pd showed the best effect due to formation of a Ni–Pd alloy (leading to speeding up of carbon migration and avoid carbon accumulation on the catalyst surface, hence extending the lifetime) [19,32,33]. Although the noble metals are active and resistant to carbon formation, but the high cost and limited availability restrict their wide applications. Previously, we investigated effects of different promoters (La, Co, Fe, Ce, and Cu) on physicochemical properties of the supported Ni catalysts, and observed that the copper addition not only prevented formation of the graphite layers on the Ni sites, but also enhanced the Ni reducibility and methane adsorption on the catalyst surface [6]. To this end, Cu as a promoter has been widely studied in the catalytic decomposition of methane [34–37]. Due to the similarity in electron structure of chromium and copper, Cr can be used as an effective promoter to achieve better activity and durability. Morris et al. [38] reported that the 10 mol% Cr_2O_3-doped ordered mesoporous alumina sample showed a significant improvement in thermal stability. On the other hand, chromium oxide could prevent the fast decrease of catalyst surface area induced by the thermal sintering under reaction conditions, and was hence used as an efficient promoter for many reactions, such as partial oxidation of methane [39], water−gas shift [40,41] and Fischer−Tropsch synthesis [42]. According to the literature, tungsten and molybdenum could play a similar role as chromium,

and the bimetallic Co–Mo- or Co–W-based catalysts were studied before. Ni et al. [43] investigated the addition of Mo to the Co/MgO catalyst, and found that formation of Mo_2C led to the drop in CH_4 dissociation rate and the Mo-doped catalyst was more stable than the Co/MgO catalyst. Awadallah et al. [44] examined the effect of 25 wt.% group VI metal (Cr, Mo or W) addition to 25 wt.% Co/MgO on catalytic decomposition of methane, and pointed out that the addition of group VI metals induced a strong interaction with the MgO and CoO_x crystals, which greatly modified the surface properties and enhanced the catalytic stability of methane decomposition.

In the present study, we examined the influence of group VIB metals (Cr, Mo, and W) on the physicochemical characteristics and methane decomposition activity of the Ni/MgO catalysts derived from a facile "one-pot" evaporation-induced self-assembly (EISA) route, and such information has not been reported in the literature.

2. Experimental

2.1. Catalyst preparation

The 55 wt.% Ni/MgO catalyst was synthesized using the "one-pot" EISA method described previously. The Ni loading of 55 wt.% was chosen according to the results of our previous works [6,26,28,29]. The typical synthesis procedures are as follows: 1.00 g of triblock copolymer (P123, $M_{Wave.} = 5800$ g/mol, Sigma Aldrich) was dissolved in 20 mL of absolute ethanol (Scharlau) under stirring at room temperature (RT). After being completely dissolved, 1.60 mL of 65 wt.% HNO_3 aqueous solution (Merck) was quickly added to the above aqueous solution. Afterwards, 1.29 g of $Ni(NO_3)_2 \cdot 6H_2O$ and 1.38 g of $Mg(NO_3)_2 \cdot 6H_2O$ were added to the above mixed solution and aged for 7 h to obtain a transparent green solution. The mixture was dried at 65 °C for 48 h and calcined in furnace at a ramp of 1 °C/min from RT to 600 °C and maintained at this temperature for 5 h, thus obtaining the mesoporous 55 wt.% Ni/MgO sample (denoted as 55Ni/MgO).

The promoted Ni-based catalysts with group VIB metals were prepared via the incipient wetness impregnation route. In a typical preparation, the 55Ni/MgO sample was impregnated with the appropriate amount of $Cr(NO_3)_3 \cdot 9H_2O$, $(NH_4)_6Mo_7O_{24} \cdot 4H_2O$ or $(NH_4)_{10}(W_{12}O_{41})$ $\cdot 5H_2O$ in ethanol solution for 4 h. After that, the mixture was dried at 80 °C for 12 h, and then calcined from RT to 500 °C and kept at this temperature for 4 h (denoted as 55Ni−Me/MgO (Me = Cr, Mo or W).

2.2. Catalyst characterization

Surface areas of the as-fabricated samples were measured using the BET method via N_2 adsorption at −196 °C on a Belsorb mini II apparatus analyzer. All of the samples were degassed at 200 °C for 3 h under vacuum before measurements. The particle sizes were obtained according to the equation: D (nm) = $6000/(\rho\ S_{BET})$, where ρ is the mean density and S_{BET} is the BET surface area of the sample. Crystal structures of the samples were determined by means of the X-ray diffraction (XRD) technique on a PANalytical X'Pert-Pro operated with Cu $K\alpha$ radiation. Hydrogen temperature-programmed reduction (H_2–TPR) was performed on a chemical adsorption analyzer (Micromeritics chemisorb 2750). In addition, the temperature-programmed oxidation (TPO) of the spent catalysts was carried out on the apparatus same as that used in the H_2–TPR experiments by introducing an oxidizing gas stream mixture with 95% He. The scanning electron microscopic (SEM) images of the samples were recorded on a Gemini Zeiss Supra 55 apparatus (operating at 10 kV). The transmission electron microscopic (TEM) images (JEOL JEM-2010 instrument) and high angle annular dark field (HAADF) and element mapping analysis images were obtained on the equipment FEI G2 80−200/Chemi-STEM Cs-corrected TEM with probe corrector. The binding energies (BEs) of O 1 s, Ni 2p, and Cr 2p of surface species were measured using X-ray photoelectron spectroscopy (XPS, ESCALAB250Xi, Thermo Scientific, UK) with Mg $K\alpha$

(hv = 1253.6 eV) as excitation source. The samples were pretreated in N_2 (flow rate = 20 mL/min) at 300 °C for 60 min to remove the adsorbed water and carbonate species on the sample surface and then samples were degassed in the preparation chamber for 30 min (10^{-5} Torr) before XPS spectrum recording. Laser Raman spectra of the samples were measured on a Horiba HR (532 nm) to characterize the accumulated carbon in the range of 0–4000 cm^{-1}.

2.3. Catalytic evaluation

Prior to the reaction, ca. 25 mg of the catalyst sample with 75 mg inert quartz sands (25 − 50 mesh) was reduced at 700 °C and atmospheric pressure using a pure hydrogen stream (20 mL/min) for 3 h in a continuous flow fixed-bed vertical quartz reactor (i.d. = 0.8 cm) operated in a down flow mode. A mixture of methane and nitrogen (15 vol% CH_4 + 85 vol% N_2) was used as feedstock. Methane decomposition over the catalysts was carried out in the range of 575 − 700 °C and at a gas hourly space velocity (GHSV) of 48,000 mL/(g h) until complete deactivation of the catalyst. The stability of the catalysts was tested at 600 and 675 °C for 10 or 5 h under the same conditions, respectively. The CH_4 conversion was monitored at regular intervals using the online gas chromatograph (Varian 3400) equipped with a thermal conductivity detector (TCD), with the Carboxen 1000 as packing column and Ar as carrier gas.

3. Results and discussion

3.1. Characterization of fresh samples

3.1.1. Pore structure and surface area

Table 1 summarizes the textural properties of the parent catalyst (55Ni/MgO) and the group VIB metal-promoted catalysts. It is obviously seen that introduction of a group VIB metal (Cr, Mo or W) to 55Ni/MgO caused a significant loss in surface area and pore volume of 55Ni–10Cr/MgO (18.2 m^2/g and 0.08 cm^3/g), 55Ni–10Mo/MgO (10.7 m^2/g and 0.05 cm^3/g), and 55Ni–10 W/MgO (7.16 m^2/g and 0.04 cm^3/g), respectively, as compared with 55Ni/MgO (31.7 m^2/g and 0.12 cm^3/g). It could be attributed to the pore plugging by the doped metals and partial collapsing of the mesoporous structure [45]. Furthermore, the average pore sizes of the samples estimated according to the BJH method were in the range of 20.2 − 14.5 nm. The lowest surface area (7.2 m^2/g) and pore volume (0.04 cm^3/g) were observed in the W-doped catalyst. In addition, it is also observed from Table 1 that the rise in Cr content gave rise to decreased BET surface area and pore volume from 23.5 m^2/g and 0.11 cm^3/g of the 55Ni − 5Cr/MgO catalyst to 16.8 m^2/g and 0.07 cm^3/g of the 55Ni − 15Cr/MgO catalyst, respectively. Such decreases in BET surface area and pore volume induced by chromium content rise could be due to a more agglomeration of catalyst particles with a higher Cr content [29]. Simultaneously, this trend was also observed for the reduced samples at 700 °C. Since the temperature of the reduction step was higher than that of the calcination process, the reduced samples showed lower BET surface areas than the calcined

ones. As can be seen from the calcined catalysts, doping Cr^{3+} and increasing the chromium content enhanced agglomeration of the nanoparticles and had a negative influence on the BET surface area, as compared with the undoped catalyst. For the spent Cr-doped catalyst, however, addition of chromium had a positive influence on stabilizing the BET surface area during the reaction, as compared with the undoped catalyst (for example, the BET surface area decreased 33 and 10% for the 55Ni/MgO and 55Ni–10Cr/MgO catalysts, respectively). This depended on the strong thermal and chemical stability of chromium, as reported in an earlier reported study that addition of chromium species to magnetite caused a strong interaction with NiO which inhibited formation of a solid solution, leading to restriction of rapid thermal sintering [46].

The porous structures of the samples were further investigated by the N_2 adsorption-desorption technique, and their isotherms are shown in Fig. 1A. According to the IUPAC classifications, each of the samples displayed a type IV isotherm (related to a mesoporous structure with cylindrical and parallel channels) with a type H1 hysteresis loop (linkable to the presence of medium size mesopores [47]) in the relative pressure (p/p_0) range of 0.7–1.0. As can be seen, the type of isotherm was not affected by the doping of the promoters, but it led to a drop in the slope of the isotherm and width of the hysteresis loop. The Mo- or W-doped sample exhibited a lower width of the hysteresis loop as compared with the undoped or Cr-doped sample, suggesting the lower surface area of the former sample. These results were in good agreement with the data in Table 1. The pore-size distributions of the samples are shown in Fig. 1B. Obviously, all of the samples displayed a pore-size distribution of 2 − 20 nm, confirming the existence of mesoporous structures. As predicted, the group VIB metal-doped samples and the samples with elevated Cr loadings decreased in peak intensity and widened in pore-size distribution, which could be attributable to the plugging of pores after doping of the promoters and local covering of the 55Ni/MgO sample by the elevated doped Cr [48]. The N_2 adsorption − desorption isotherms and pore-size distributions of the reduced samples are also shown in Fig. 1C and D. Formation of a hysteresis loop (Fig. 1C) in N_2 adsorption − desorption isotherms indicates the presence of mesopores in the reduced catalysts. Furthermore, the isotherms were type IV with a H1 hysteresis loop, which confirms the presence of a mesostructure. As can be seen from Fig. 1D, the reduced samples displayed slightly wider pore-size distributions than the calcined samples.

3.1.2. Crystal structure

Crystal phases of the 55Ni/MgO and Cr-, Mo-, and W-doped samples were determined by the XRD technique, and their XRD patterns are shown in Fig. 2. Each sample presented Bragg diffraction peaks at 2θ = 37.3°, 43.4°, 63.0°, 75.6°, and 79.3°, which was assigned to the (111), (200), (220), (311), and (222) crystal planes of the cubic NiO structure (JCPDS PDF# 01-073-1519). Also, there was a small peak located at 27.5°, which was related to the Ni$_2$O$_3$ phase (JCPDS PDF# 014-0481) [49]. Nevertheless, no apparent diffraction peaks attributable to the Mg, Cr, Mo, and W phases were recorded. This observation was

Table 1
BET surface areas, pore volumes, pore sizes, and NiO crystal sizes of the undoped and group VIB metal-doped 55Ni/MgO samples.

Sample	BET surface area (m^2/g)			Pore volume (cm^3/g)			Pore size (nm)			Particle size (nm)	H$_2$ consumption (mmol/g)[a]	Mean NiO crystal size (nm)	Mean Ni crystal size (nm)
	Calcined	Reduced	Spent	Calcined	Reduced	Spent	Calcined	Reduced	Spent				
55Ni/MgO	31.7	21.4	14.3	0.12	0.14	0.29	14.6	20.9	22.4	29.0	12.48	23.2	15.7
55Ni − 5Cr/MgO	23.5	21.9	17.6	0.11	0.11	0.21	18.2	21.2	21.6	38.1	11.77	22.1	18.9
55Ni − 10Cr/MgO	18.2	17.1	15.3	0.08	0.10	0.22	17.9	21.7	23.2	47.9	14.56	24.0	23.5
55Ni − 15Cr/MgO	16.8	14.9	11.5	0.07	0.10	0.25	14.5	19.6	22.7	50.6	14.13	25.1	19.8
55Ni − 10Mo/MgO	10.7	5.6	–	0.05	0.09	–	18.8	27.4	–	96.6	12.92	23.5	12.8
55Ni − 10W/MgO	7.2	5.8	–	0.04	0.07	–	20.2	29.1	–	69.7	8.57	23.3	10.3

[a] H$_2$ consumption obtained after quantitative analysis of the reduction peaks in TPR profiles shown in Fig. 3.
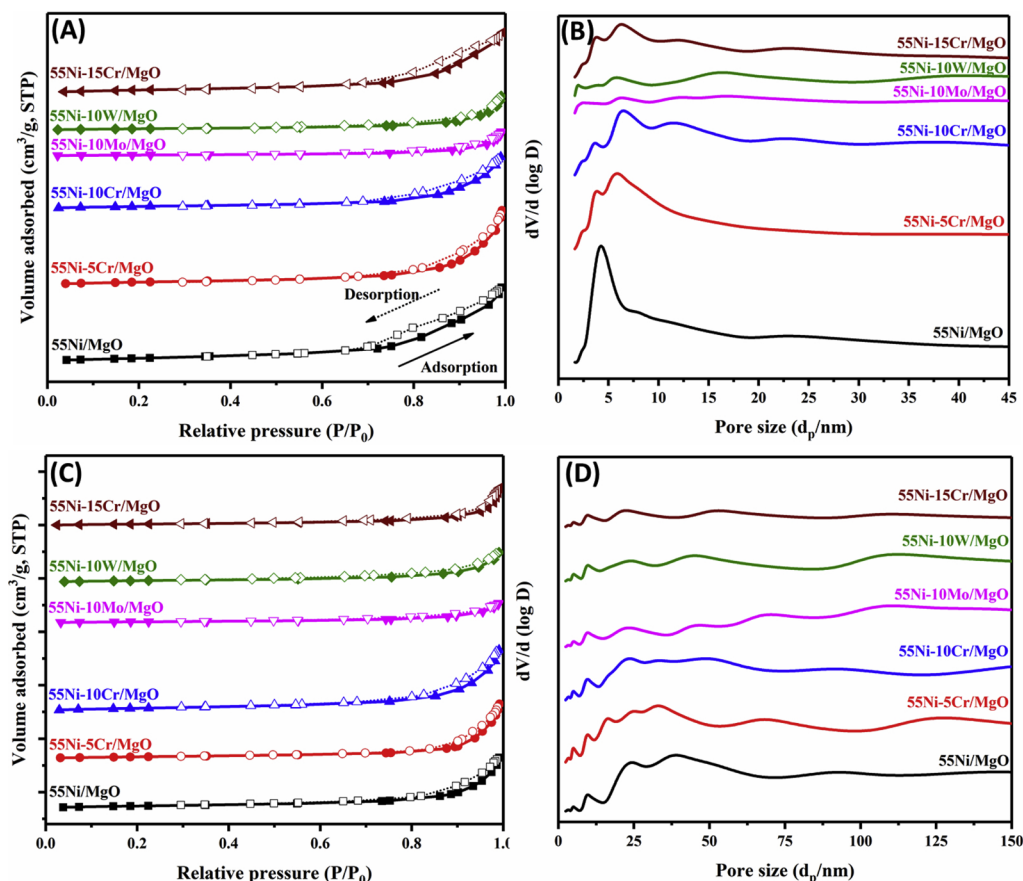
Fig. 1. Nitrogen adsorption − desorption isotherms and pore-size distributions of the (A,B) calcined and (C,D) reduced undoped and group VIB metal-doped 55Ni/MgO samples.

probably due to the two reasons: (i) the diffraction peaks of MgO (JCPDS PDF# 01-1235) and NiCr$_2$O$_4$ (JCPDS PDF# 01-088-0109) were overlapped with the NiO phase peaks; and (ii) Mo and W were amorphous and/or well dispersed in the sample. That is to say, the loading of Mo and W did not result in an obvious change in crystal structure of NiO [13,50]. As mentioned, the diffraction peaks of the NiCr$_2$O$_4$ were overlapped with nickel oxide phase. The introduction of chromium to 55Ni/MgO gave rise to a higher crystallinity as compared with the undoped sample. This can be ascribed to the interaction of CrO − NiO, which could increase the peak intensity of NiO phase in XRD pattern. In addition, the rise in Cr doping from 5 to 15 wt.% obviously increased the crystallinity. According to the Scherrer equation ($D = 0.89\lambda/(\beta \cos$

(θ)), where λ is the X-ray wavelength, β is the mean full width at half maximum (FWHM) of NiO, and θ is the diffraction angle), the grain sizes (crystallite sizes (D)) of NiO in the samples were calculated, as summarized in Table 1. The results demonstrate that the estimated grain sizes of 23.2, 23.5, and 23.3 nm of NiO crystallites in the 55Ni/MgO, 55Ni − 10Mo/MgO, and 55Ni − 10 W/MgO samples were much similar, but those in the Cr-doped samples increased from 22.1 to 25.1 nm with Cr loading from 5 to 15 wt.%. The XRD patterns of the 700 °C-reduced catalysts are shown in Fig. 2B. The diffraction peaks at $2\theta = 44.6°$, $52.0°$, and $76.5°$ were assigned to the (111), (200), and (220) crystal planes (JCPDS PDF# 01-087-0712) with an average Ni crystal size of $13.3 − 22.5$ nm. This result confirms that the NiO was
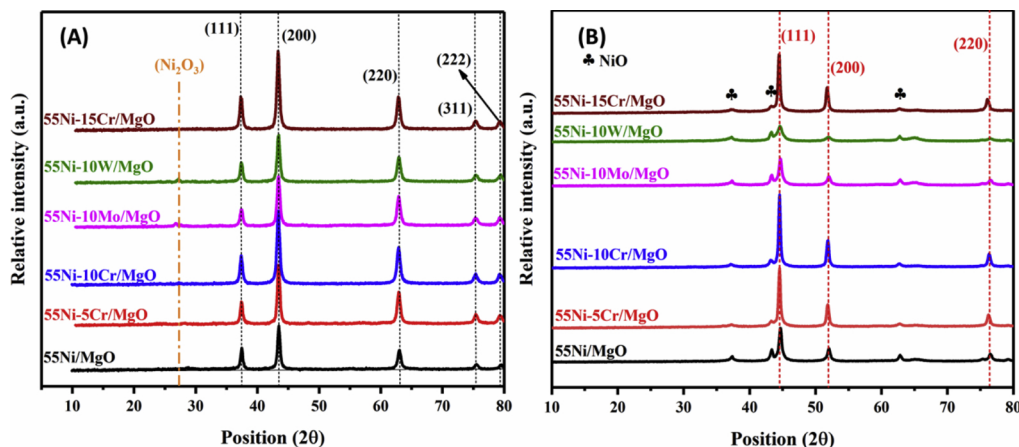

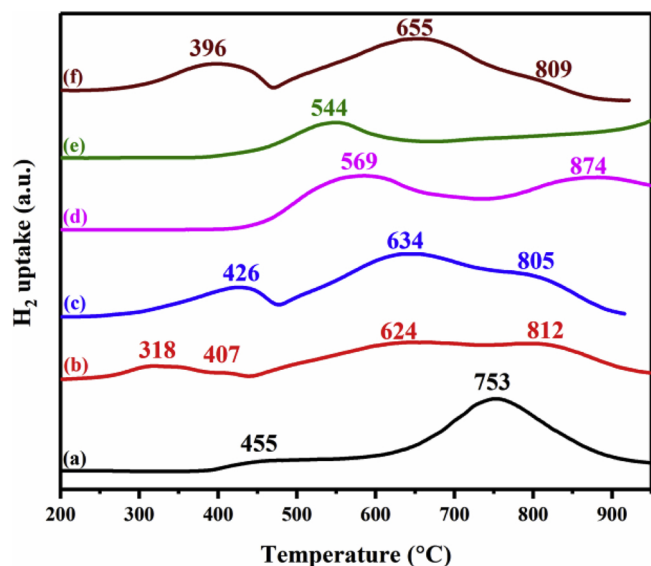**Fig. 2.** XRD patterns of the (A) calcined and (B) reduced undoped and group VIB metal-doped 55Ni/MgO samples.

Fig. 3. H_2-TPR profiles of (a) 55Ni/MgO, (b) 55Ni − 5Cr/MgO, (c) 55Ni − 10Cr/MgO, (d) 55Ni − 10Mo/MgO, (e) 55Ni − 10 W/MgO, and (f) 55Ni − 15Cr/MgO.

converted to metallic nickel during the H_2-reduction process, and doping chromium and increasing its content increased the average Ni crystal size.

3.1.3. Reducibility

H_2-TPR technique was used to investigate the effect of group VIB metal introduction on the reducibility of the 55Ni/MgO sample, and their profiles are illustrated in Fig. 3. The 55Ni/MgO sample displayed two main reduction peaks centered at 455 and 753 °C: the low-temperature peak at 455 °C was attributed to the reduction of nickel oxide in the sample, whereas the high-temperature peak at 753 °C was due to the reduction of NiO that interacted with MgO to form the NiO − MgO solid solution. Similar results were also reported previously [51]. The 55Ni–5Cr/MgO sample showed three reduction peaks, followed by a broad feature at high temperature centered at 812 °C. The first peak at 477 °C was mainly attributed to the reduction of Cr^{6+} to Cr^{4+} [41], the weak peak at 407 °C was associated with the reduction of the bulk nickel oxide, the peak at 624 °C might be due to the reduction of NiO with a moderate interaction (i.e., $NiCr_2O_4$ or $MgCr_2O_4$), and the broad reduction peak at a temperature higher than 812 °C was related to the reduction of the NiO–MgO solid solution [52]. It is clearly observed that addition of Cr improved the reducibility of the Ni species and shifted the T_{max} to a lower temperature, as compared with the 55Ni/MgO sample. Furthermore, the rise in Cr loading from 5 to 15 wt.% resulted in an increase in intensity of the reduction peak, indicating a higher H_2 consumption as compared with the Cr-free sample. The 55Ni–10Mo/MgO sample exhibited two reduction peaks. The first peak at 569 °C was due to the reduction of the non-interacting NiO phase as well as the reduction of Mo^{6+} to Mo^{4+} species [53,54]. This peak was shifted to a higher temperature as compared with the 55Ni/MgO sample, possibly due to the fact that an appreciable part of the NiO species was consumed to form $NiMoO_4$. Furthermore, the combination of MoO_x with NiO could prevent the reduction of the nickel species. It might be related to the fact that the Mo^{6+} polarized the Ni–O bonds, making them more ionic and therefore more difficult to be reduced [55]. The second peak centered at 780 °C was attributed to the reduction of $NiMoO_4$ associated with the hard reduction of molybdenum ($Mo^{6+} \rightarrow Mo^{4+}$) or related to the reduction of the $MgMoO_4$ phase. In the case of the W-doped sample, the peak centered at 544 °C corresponded to the reduction of bulk NiO, whereas the broad peak that started at a temperature above 900 °C or even up to above 950 °C was associated with the reduction of WO_3 and $MgWO_4$ as well as part of the $NiWO_4$ species (confirming the hard reducibility of these species [56]). Meanwhile, the reduction temperature of this sample well agreed with the results of previous work [57]. It is concluded that the low-temperature H_2 consumption of the Cr-doped samples was higher than that of the Mo- and W-doped samples (Table 1). Furthermore, the Cr-doped samples with higher surface areas consumed more amounts of H_2 during the reduction process at low temperatures, resulting in the significant NiO reduction and subsequently increase in catalytic performance for methane decomposition.
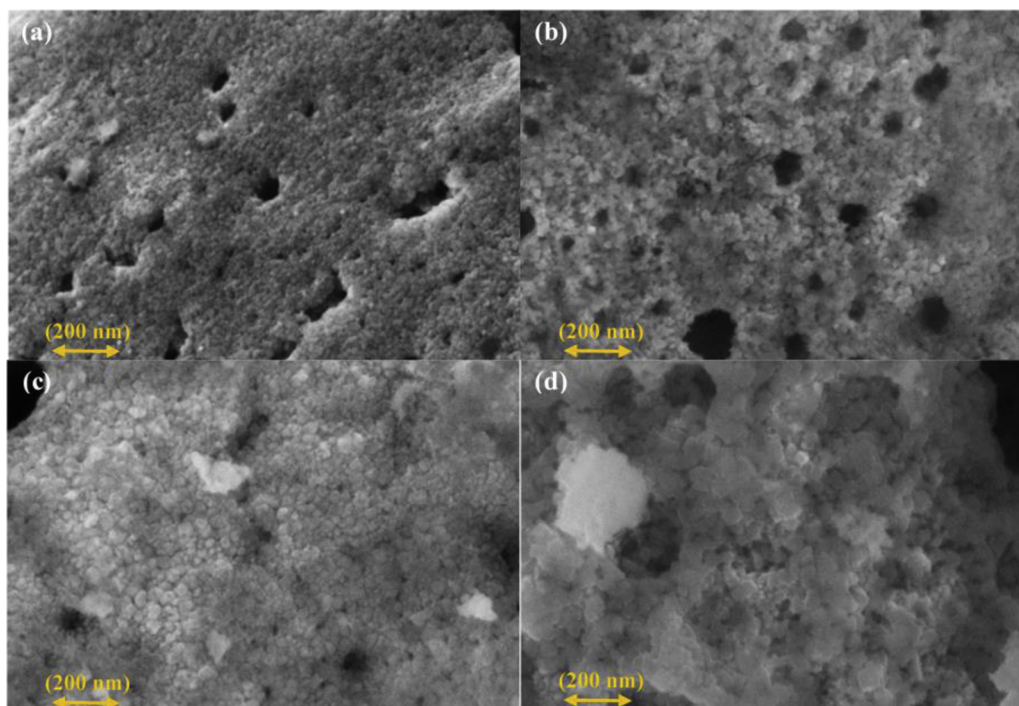

Fig. 4. SEM images of (a) 55Ni/MgO, (b) 55Ni − 5Cr/MgO, (c) 55Ni − 10Cr/MgO, and (d) 55Ni − 15Cr/MgO.
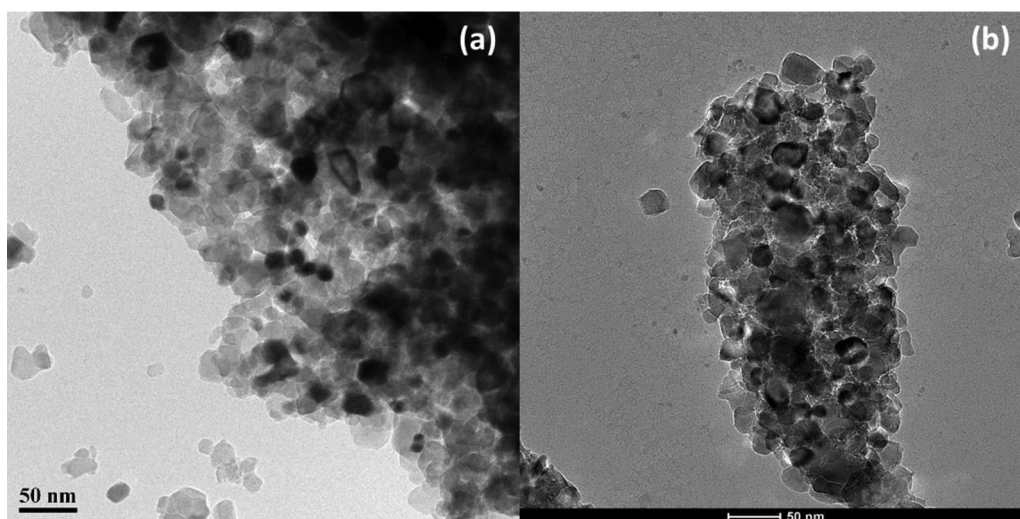
Fig. 5. TEM images of (a) 55Ni/MgO and (b) 55Ni−10Cr/MgO.

3.1.4. Morphology

According to the SEM (Fig. 4) and TEM (Fig. 5) images of undoped and Cr-doped 55Ni/MgO samples, we can see that all of the samples obtained after calcination at 600 °C exhibited a mesoporous architecture and the sizes of the particles in the samples were lower than 50 nm. After introduction of Cr, as can clearly be observed in the TEM images, the samples maintained a morphological feature similar to that of the Cr-free sample. With the rise in Cr loading, however, the particle slightly grew and the 55Ni−15Cr/MgO sample possessed the largest particles owing to agglomeration of the particles after the doping of Cr. On the other hand, due to the introduction of chromium oxides to the sample, the porosity declined, which was also shown by textural property of the parent sample (Table 1). We made an elemental analysis on the 55Ni−10Cr/MgO sample, as shown in Fig. 6. The existence of Ni, Mg, and Cr with no impurities confirms the Ni, Cr, and Mg elements were highly distributed on the surface of the sample.

3.1.5. Surface composition, Ni oxidation state, and oxygen species

X-ray photoelectron spectroscopy (XPS) is an effective technique for measuring the surface chemical composition, and metal oxidation states of a solid oxide material, what is necessary to determine the chemical status of the catalytic active species, while XRD only is a bulk technique. Fig. 7 illustrates the O 1 s, Ni 2p and Cr 2p XPS spectra of the Cr-doped 55Ni/MgO samples with different Cr loadings and Table 2

summarizes the main peaks of the O 1 s, Ni $2p_{3/2}$ and Cr $2p_{3/2}$ energy levels and quantitative analysis results. Table 2 also lists the surface element compositions of the 55Ni−5Cr/MgO, 55Ni−10Cr/MgO, and 55Ni−15Cr/MgO catalysts determined by the XPS technique. The concentration of O_{ads} on the surface of the 55Ni−10Cr/MgO sample was higher, probably due to a substantial contribution of oxygen from adsorbed oxygen species on the surface, which was confirmed by the higher $O_{ads}/(O_{ads} + O_{latt})$ molar ratio on this sample. Fig. 7A shows the asymmetrical O1 s spectrum, which could be deconvoluted into three components at BE ≅530.4, 531.0, and 533.0 eV, being characteristic of the surface lattice oxygen (O_{latt}) with metals in the mixed oxides, adsorbed oxygen species (O_{ads}), and bound water (H-O-H), respectively. According to the results summarized in Table 2, the surface $O_{ads}/(O_{ads} + O_{latt})$ molar ratio (0.29) of the 55Ni−10Cr/MgO sample was higher than that 0.23 and 0.22 of the 55Ni-5Cr/MgO and 55Ni-15Cr/MgO samples, respectively. It has reported that a catalyst with a higher O_{ads} concentration is more beneficial for the reduction–oxidation processes. Therefore, 55Ni−10Cr/MgO catalyst was predictable to be active and stable for the catalytic methane decomposition [26]. Furthermore, Fig. 7B and C shows the Ni 2p and Cr 2p XPS spectra of the samples, respectively. The Ni 2p spectrum was fitted with the surface Ni^{2+} and Ni^{3+} species as well as two conspicuous shake-up satellite peaks that indicates the presence of mixed oxidation states of nickel. Additionally, as shown in Table 2, the BE of the Ni^{2+} level with increasing the Cr
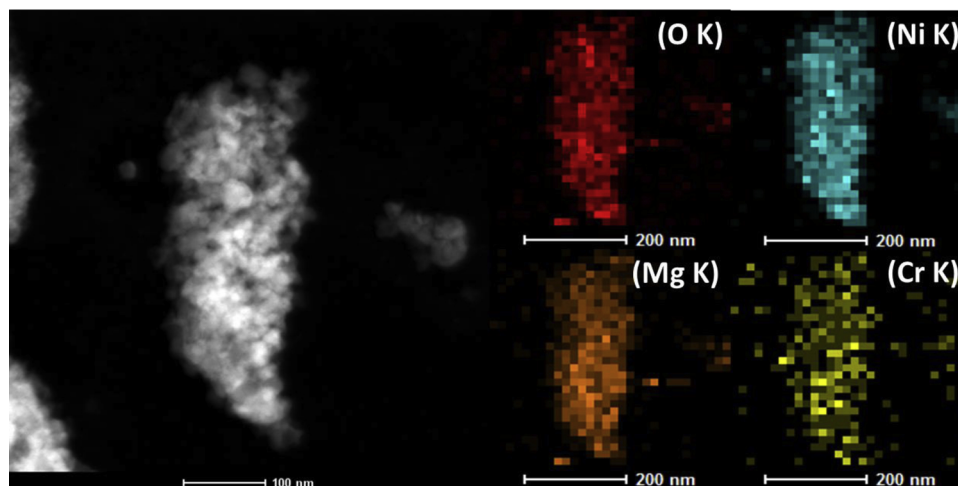

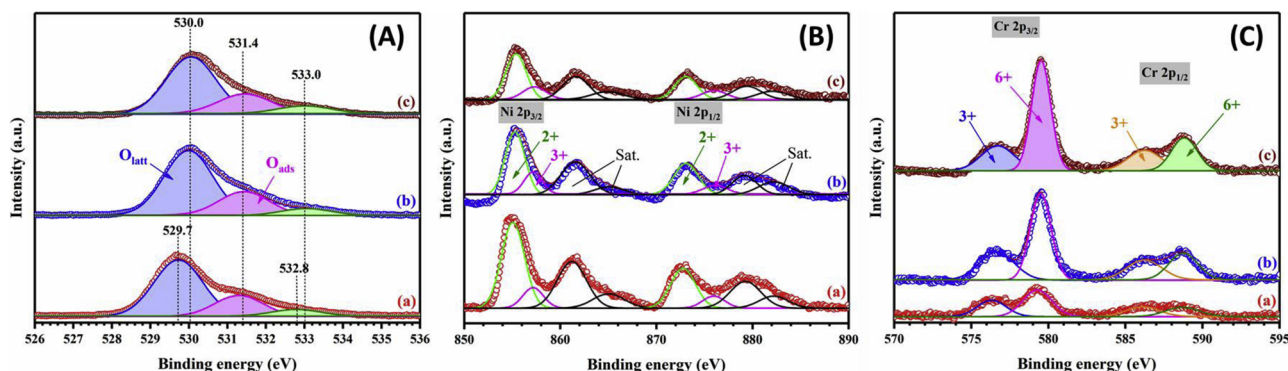**Fig. 6.** HAADF-STEM and elemental analysis images of the 55Ni−10Cr/MgO sample.

Fig. 7. (A) O 1 s, (B) Ni $2p_{3/2}$, and (C) Cr $2p_{3/2}$ XPS spectra of the a) 5%, b) 10%, and c) 15% Cr-doped 55Ni/MgO samples.

loading appeared at higher values. This reveals the presence of a strong metal−support interaction between Ni and MgO that could change the electronic and structural properties of nickel. This higher value also was in accordance with the H_2-TPR results (Fig. 3), which led to a harder reducibility of Ni in these samples. The spectra of Cr 2p could be decomposed into the Cr $2p_{1/2}$ and Cr $2p_{3/2}$ signals, indicating that the chromium existed in Cr^{3+} [3]. Finally, as it was expected, the intensity of the Cr 2p signal increased by increasing their loadings because of the existence of more Cr on the surface. According to the XPS spectra, we can calculate the surface element compositions of the samples. It is well known that Cr^{3+} possesses a good oxygen storage/release ability due to the presence of chromium ions with mixed oxidation states, which facilitates the redox process of $Cr^{3+} \leftrightarrow Cr^{6+}$. Adsorbed oxygen species are associated with the number of oxygen vacancies, which are helpful for the activation of oxygen molecules [58]. In addition, the adsorbed oxygen species concentration was also related to the adsorption and/or activation of methane molecules [59]. Therefore, a higher adsorbed oxygen species concentration would be favorable for the decomposition of methane.

3.2. Catalytic performance and stability

Fig. 8A presents the conversions of methane in a stepwise heating mode from 575 to 700 °C over the 55Ni/MgO and group VIB metal-doped samples. All of the samples showed the maximum initial methane conversions at 575 °C, and methane conversion decreased with a rise in temperature even though methane decomposition is an endothermic reaction. Such a phenomenon might be due to agglomeration of the particles and covering of the active sites by the deposited carbon at high temperatures [36]. A comparison on catalytic activity of the undoped and group VIB metal-doped samples indicates that only chromium doping improved the activity of the 55Ni/MgO sample. According to the XRD and H_2-TPR results, the enhanced catalytic activity of the Cr-doped sample was associated with its improved reducibility and formation of a bigger crystal size. On the other hand, the 55Ni/MgO sample was completely deactivated in the range of 575 − 700 °C, while the group VIB metal-doped samples were still active in such a temperature range. These results indicate that the addition of group VIB metals could modify the stability of the 55Ni/MgO sample at high

temperatures, which was attributed to a strong metal−support interaction (as demonstrated by the H_2-TPR results). For better comparison, it should be mentioned that in the previous literature [15,16,28,35] the Ni-Cu catalysts presented a noteworthy improvement in catalytic performance and lifetime (especially at high temperatures), but doping of Cu decreased the initial CH_4 conversion below 900 °C due to inactivity of the copper in methane decomposition in the temperature range [6]. However, the existence of Cr improved the activity more significantly than the Cu-doped sample because of a more reactivity of Cr than Cu at lower temperatures. Fig. 8A also shows that methane conversion and catalyst lifetime improved with the rise in Cr loading up to 10 wt.%, a result possibly due to the better reducibility of the Cr-doped sample. Further rise in Cr doping (15 wt.%) decreased the activity, a result owning to the dramatic drop in surface area (Table 1) and the sintering of the particles. In addition, the turnover frequency (TOF_{NiO} and $TOF_{Cr_2O_3}$) was calculated based on the activity data and per gram of NiO and Cr_2O_3 in different Cr-doped samples according to the reported method [60,61]. The TOF ($mol/(g_{NiO \, or \, Cr_2O_3} \, min)$) was calculated according to the number of CH_4 molecules converted by the NiO or Cr_2O_3 sites per minute. The TOF_{NiO} and $TOF_{Cr_2O_3}$ of the samples were calculated under the conditions of CH_4/N_2 volumetric ration = 15 : 85 and GHSV = 48,000 mL/(g h), and reaction temperature = 600 °C. The results are summarized in Table 3.

Fig. 8B and C shows the comparison on catalytic lifetime and activity of the group VIB metal-doped samples at 600 and 675 °C within 10 and 5 h of methane decomposition, respectively. The initial activity over all of the samples increased with the rise in temperature from 600 to 675 °C. For example, methane conversion over 55Ni − 10Cr/MgO shifted from 68 to 87%. As predicted, the 55Ni − 10Cr/MgO sample possessed the highest stability among all of the samples, and methane conversion increased by ca. 10% at both reaction temperatures, as compared with that over Ni/MgO. After working on CH_4 decomposition over 25 wt.% Co − 25 wt.% M (M = Cr, Mo, and W)/MgO, Awadallah et al. [44] reported the methane conversion of 80% at 700 °C over the 25 wt% Co − 25 wt.% Cr/MgO sample. Wang and Lua [62] observed the highest CH_4 conversion of ca. 82% at 750 °C over the Ni − Cu alloy catalyst. Pudukudy et al. [12] claimed a maximum hydrogen yield of ca. 57% over the Ni − Pd/MgAl₂O₄ catalyst at 700 °C. By comparing our and literature's results, we can see that the as-fabricated samples would

Table 2
Binding energies of the O 1s, Ni 2p and Cr 2p levels for the Cr-doped 55Ni/MgO samples and $O_{ads}/(O_{ads} + O_{latt})$ and Cr^{3+}/Cr^{6+} molar ratios.

| Catalyst	Atomic concentration of elements on the surface determined by XPS (at%)					O 1 s (eV)		Ni $2p_{3/2}$ (eV)		Cr $2p_{3/2}$ (eV)		$O_{ads}/(O_{ads} + O_{latt})$ molar ratio	Cr^{3+}/Cr^{6+} molar ratio
	Mg	C	O	Ni	Cr	O_{ads}	O_{latt}	Ni^{2+}	Ni^{3+}	Cr^{3+}	Cr^{6+}		
55Ni − 5Cr/MgO	15.2	20.2	47.9	14.0	2.7	531.36	529.74	855.18	857.21	576.54	579.42	0.23	0.61
55Ni − 10Cr/MgO	13.4	22.5	49.0	9.7	5.4	531.45	529.98	855.29	857.21	576.62	579.50	0.29	0.54
55Ni − 15Cr/MgO	11.7	25.5	48.6	7.8	6.0	531.44	530.09	855.40	857.43	576.73	579.53	0.22	0.40
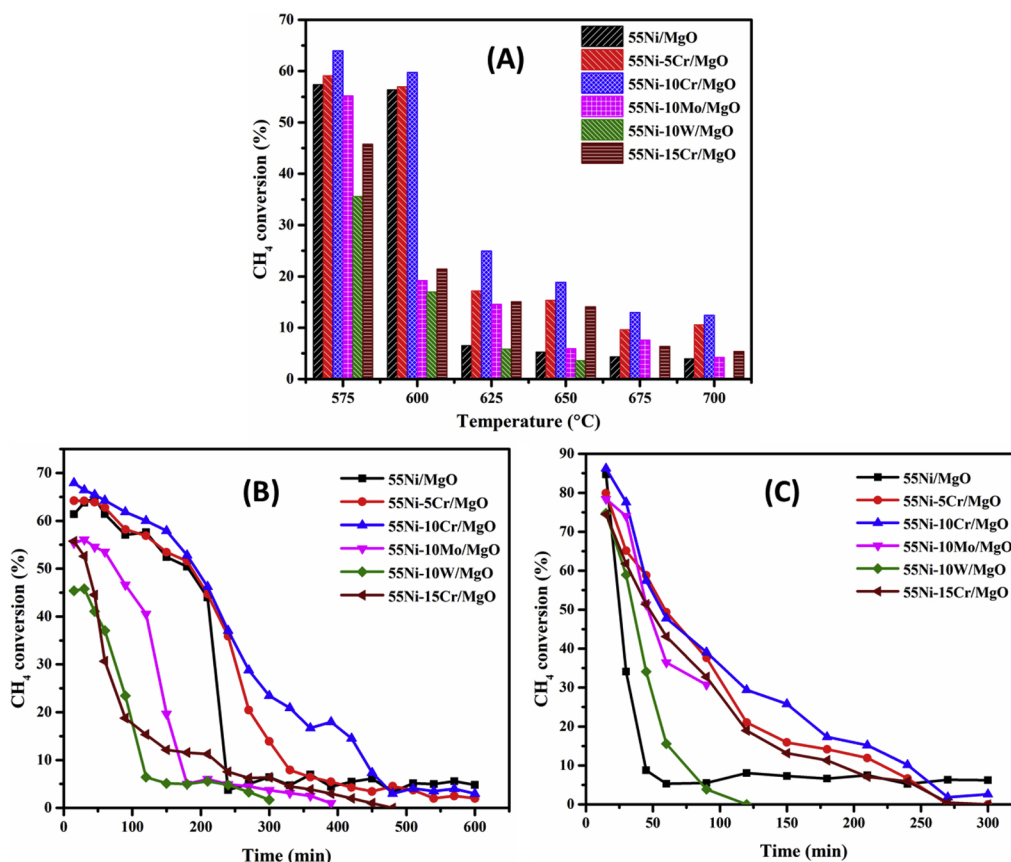
Fig. 8. (A) Correlation between methane conversion and reaction temperature and (B) and (C) stability tests at 600 and 675 °C, respectively. Reaction conditions: $CH_4 : N_2$ volumetric ratio = 15 : 85, GHSV = 48,000 mL/(g h).

Table 3
TOF values for CH_4 decomposition at 600 °C under the reaction conditions of the CH_4/N_2 volumetric ration = 15 : 85 and GHSV = 48,000 mL/(g h).

Sample	TOF_{NiO} (mol/(g_{NiO} min))	$TOF_{Cr_2O_3}$ (mol/($g_{Cr_2O_3}$ min))
55Ni/MgO	0.36	–
5Ni−5Cr/MgO	0.48	3.45
55Ni−10Cr/MgO	0.61	4.43
55Ni−15Cr/MgO	0.22	1. 93

have a high potential application for the decomposition of methane to pure hydrogen. It should be noted that the deactivation rate at 675 °C was higher than that at 600 °C, a result due to increase in carbon accumulation rate and agglomeration of the particles at high temperatures [63].

3.3. Characterization of the spent samples

The filamentous (nanofibers) characters of the carbon produced over the undoped and 10 wt.% Cr-doped 55Ni/MgO samples at 600 °C after the long-term reaction are illustrated by the SEM and TEM images in Figs. 9 and 10, respectively. As mentioned before, the deposited carbon led to an increase in pressure drop and deactivation of the catalyst [2]. Fig. 9 clearly reveals a dense population of entangled carbon filaments. The growing directions of the carbon were rather random, which might be due to the space competition during carbon growth. Therefore, determination of the carbon fiber lengths was difficult since the filaments were in an interweaving form [64]. A comparison on the images of undoped and Cr-doped samples indicates that the average diameter and amount of the carbon nanofibers increased by Cr doping, i.e., a more amount of methane decomposed over the

55Ni−10Cr/MgO sample, which was in accordance with the results obtained in the activity and stability tests in Fig. 8. It is worth to note that a catalyst particle located at the tip of a fiber (as marked in Fig. 9a), indicating that the fiber began to grow from the metal particle. In addition, as can be observed in the high-resolution TEM images (Fig. 10b and d), the average diameters of the carbon nanofibers were lower than 50 nm.

To study the nature and amounts of carbon formed during the methane decomposition process, TPO analyses on the spent Cr-, Mo-, and W-doped 55Ni/MgO samples were performed, and their profiles are shown in Fig. 11. As illustrated in our earlier works [6,26–29], in all of the cases except over the W-doped sample, the sharp peak at ca. 700 °C indicates the fast oxidation of graphitic carbon. The fast oxidation of the carbon during the TPO analysis gave rise to a high amount of produced gas, which led to a rapid and intense change in TCD signal. The used 55Ni−10 W/MgO sample showed small signals that were assigned to the low ability to decompose CH_4, as mentioned in the catalytic performance and stability section. In addition, the highest amounts of coke were achieved over the Cr-doped samples, especially over the 55Ni−10Cr/MgO sample. The increase in amount of carbon deposited by chromium doping was in agreement with the result obtained in the stability test after 600 min of on-stream reaction at 600 °C (Fig. 8b), which means that more amounts of hydrogen and carbon were produced from methane decomposition.

Raman spectroscopic technique was used to investigate the crystallinity and graphitization degree of the as-produced filamentous carbon over the spent 55Ni/MgO and Cr-doped samples after 10 h of on-stream reaction at 600 °C. As clearly observed in Fig. 12, the band positions of the Raman spectra remained unchanged after Cr doping, indicating the same nature and morphology of the deposited carbon. All of the Raman spectra displayed four characteristic bands. The D-band
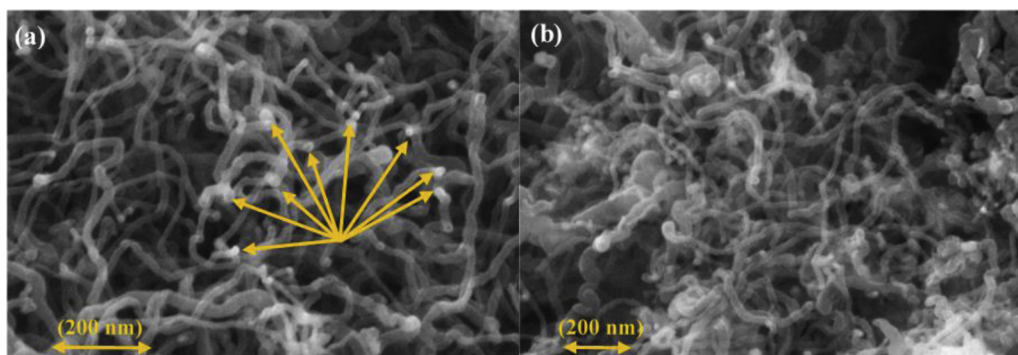
Fig. 9. SEM images of the spent (a) undoped and (b) 10 wt.% Cr-doped 55Ni/MgO samples. Reaction conditions: reaction temperature = 600 °C, CH$_4$: N$_2$ volumetric ratio = 15 : 85, reaction time = 600 min, and GHSV = 48,000 mL/(g h).

(1335–1345 cm^{-1}) was attributed to the disordered carbon species with the vibration of sp^3 hybridized carbon atom [65]. The G-band at around 1590 cm^{1-} was due to the existence of carbon atom mode with sp^2 hybridized carbon networks in the ordered graphite [66]. It was reported that the peak area ratio (I$_D$/I$_G$) of the D- and G-bands could be referred to the crystallinity (graphitization) degree and the presence of imperfection in the carbon species, and the near unit value indicates that the carbon species were highly graphitized [47]. The 55Ni/MgO sample exhibited the highest I$_D$/I$_G$ value of 1.69, representing that the

poorest crystallinity of filamentous carbon was obtained over this sample. Conversely, the I$_D$/I$_G$ values were found to decrease with introducing chromium to the 55Ni/MgO sample. There were more amounts of graphitic carbon over the Cr-doped catalysts, which could be attributed to the high structural imperfection in 55Ni/MgO, as compared with the Cr-doped samples [67]. In addition, the I$_D$/I$_G$ values were 0.89, 0.97, and 0.84 over the 5, 10, and 15 wt.% Cr-doped 55Ni/MgO samples, respectively. Therefore, formation of the coke with different crystallinity could occur over the Cr-doped samples with
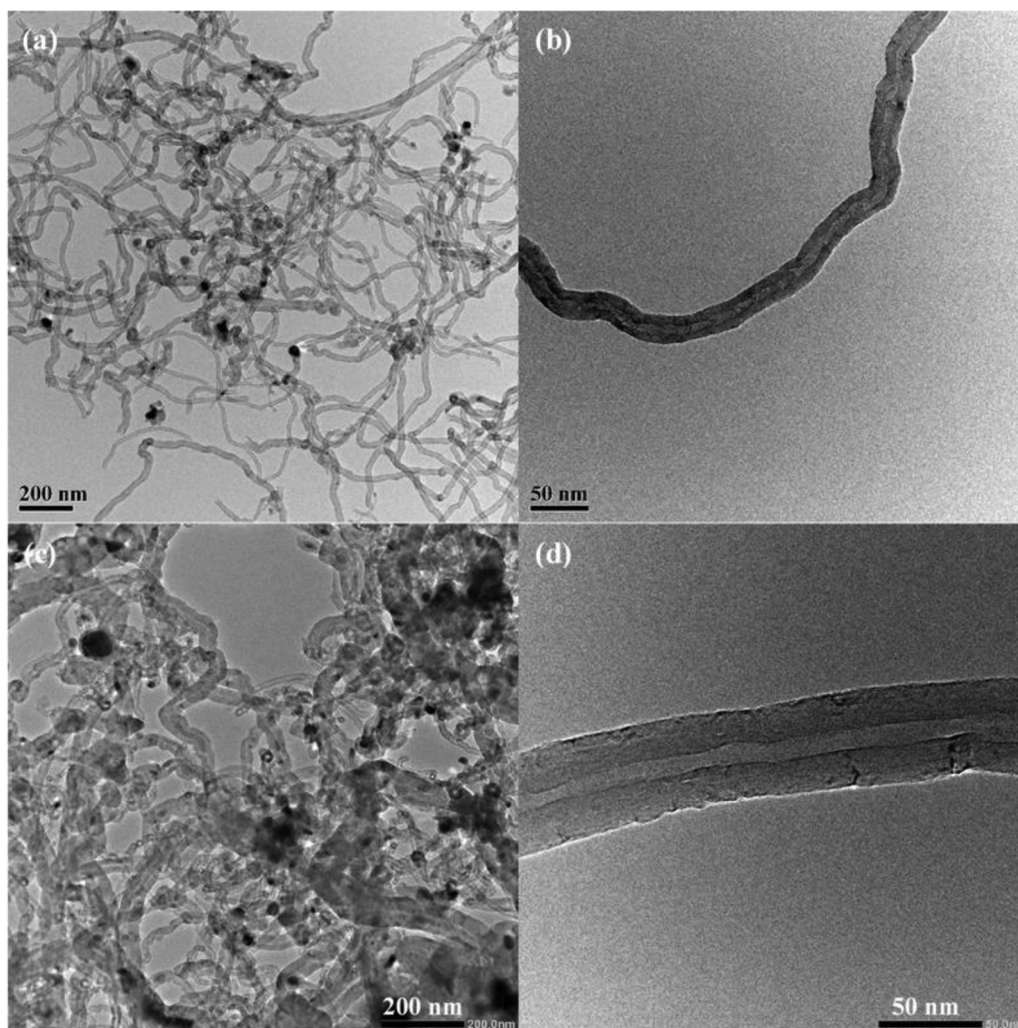

Fig. 10. TEM images of the spent (a, b) undoped and (c, d) 10 wt.% Cr-doped 55Ni/MgO samples. Reaction conditions: reaction temperature = 600 °C, CH$_4$: N$_2$ volumetric ratio = 15 : 85, reaction time = 600 min, and GHSV = 48,000 mL/(g h).
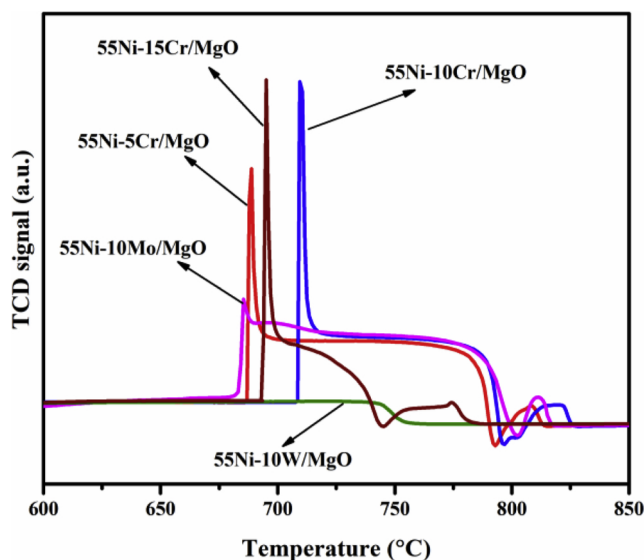
Fig. 11. TPO profiles of the spent 55Ni/MgO and VIB group metal-doped 55Ni/MgO samples. Reaction conditions: Reaction temperature = 600 °C and reaction time = 600 min.
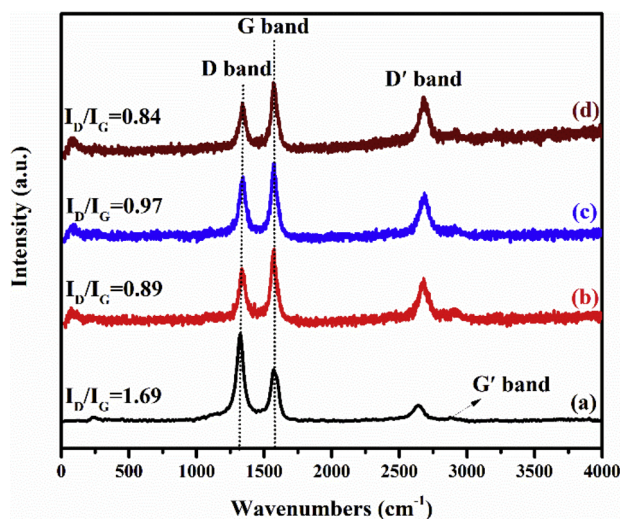

Fig. 12. Raman spectra of the carbon deposited over (a) 55Ni/MgO, (b) 55Ni−5Cr/MgO, (c) 55Ni−10Cr/MgO, and (d) 55Ni−15Cr/MgO after 10 h of on-stream reaction at 600 °C.

different Cr doping. These data agreed with the catalytic performance of the 55Ni−10Cr/MgO sample, over which methane decomposition was less deactivated than over the other samples. As reported in the earlier literature, the encapsulated and disordered carbon could cover the surface of the active centers and led to the deactivation of the catalyst [6]. The two bands that appeared at 2655 and 2910 cm^{-1} were assigned to the graphene layers (the single-layered graphene sheets) in 2D two-phonon route (labeled D′ and G′ bands, respectively). Due to the low intensity of the two bands as compared with that of the D- and G-bands, the D′- and G′-bands only reveal formation of the few layered graphene sheets [68].

4. Conclusions

In this work, the 55Ni/MgO and group VIB metal-doped catalysts were prepared using a facile one-pot evaporation-induced self-assembly and impregnation methods, respectively. The influence of the group VIB metals (Cr, Mo and W) doped to the 55Ni/MgO sample on the activity

and stability in the catalytic decomposition of methane was investigated. Addition of an appropriate amount of chromium greatly enhanced the performance and stability of the 55Ni/MgO catalyst, with the 55Ni−10Cr/MgO sample showing the highest catalytic activity (CH$_4$ conversion = 87% at 675 °C and GHSV = 48,000 mL/(g h)) and good thermal stability at 600 or 675 °C. Based on the activity data and characterization results, it is concluded that the better catalytic performance of 55Ni−10Cr/MgO was associated with its higher surface area, higher oxygen adspecies concentration, and better reducibility. According to the results of deposited carbon nature and TEM, TPO and Raman characterization results, one can realize that multi-walled filamentous carbon was formed over all of the catalysts, among which the carbon generated over 55Ni−10Cr/MgO exhibited higher crystallinity and purity as well as degree of crystallinity. We are sure that the Cr-doped 55Ni/MgO catalyst would work well in the on-board H$_2$ production from the catalytic decomposition of methane in PEMFCs.

Prime novelty statement

In this work, the doping of a group VIB metal (Cr, Mo or W) to the 55Ni/MgO catalyst was investigated in detail on the structural property and catalytic activity for the decomposition of methane. The 55Ni/MgO catalyst was successfully synthesized by a facile simultaneous "one-pot" evaporation-induced self-assembly (EISA) method. The results indicate that these catalysts performed well for methane decomposition and the Cr-doped samples showed better catalytic performance and stability. This relationship of the current catalysts may give a useful reference in designing the catalysts for the production of highly pure hydrogen from methane decomposition.

Acknowledgements

References

[1] X. Li, D. Li, H. Tian, L. Zeng, Z.J. Zhao, J. Gong, Dry reforming of methane over Ni/La$_2$O$_3$ nanorod catalysts with stabilized Ni nanoparticles, Appl. Catal. B 202 (2017) 683–694.

[2] A.C. Lua, H.Y. Wang, Hydrogen production by catalytic decomposition of methane over Ni-Cu-Co alloy particles, Appl. Catal. B 156–157 (2014) 84–93.

[3] L. Yang, L. Pastor-Pérez, S. Gu, A. Sepúlveda-Escribano, T. Reina, Highly efficient Ni/CeO$_2$-Al$_2$O$_3$ catalysts for CO$_2$ upgrading via reverse water-gas shift: effect of selected transition metal promoters, Appl. Catal. B 232 (2018) 464–471.

[4] J.H. Lunsford, Catalytic conversion of methane to more useful chemicals and fuels: a challenge for the 21st century, Catal. Today 63 (2000) 165–174.

[5] M. Pudukudy, Z. Yaakob, M. Mohammad, B. Narayanan, K. Sopian, Renewable hydrogen economy in Asia–opportunities and challenges: an overview, Renew. Sustain. Energy Rev. 30 (2014) 743–757.

[6] A. Rastegarpanah, F. Meshkani, M. Rezaei, CO$_x$-free hydrogen and carbon nanofibers production by thermocatalytic decomposition of methane over mesoporous MgO·Al$_2$O$_3$ nanopowder-supported nickel catalysts, Fuel Process. Technol. 167 (2017) 250–262.

[7] C. García-Sancho, R. Guil-López, L. Pascual, P. Maireles-Torres, R. Navarro, J. Fierro, Optimization of nickel loading of mixed oxide catalyst ex-hydrotalcite for H$_2$ production by methane decomposition, Appl. Catal. A Gen. 548 (2017) 71–82.

[8] A.C. Lua, H.Y. Wang, Decomposition of methane over unsupported porous nickel and alloy catalyst, Appl. Catal. B 132–133 (2013) 469–478.

[9] J.N. Armor, Catalysis and the hydrogen economy, Catal. Lett. 101 (2005) 131–135.

[10] G. Wang, Y. Jin, G. Liu, Y. Li, Production of hydrogen and nanocarbon from catalytic decomposition of methane over a Ni–Fe/Al$_2$O$_3$ catalyst, Energy Fuels 27 (2013) 4448–4456.

[11] U. Ashik, W.W. Daud, H.F. Abbas, Production of greenhouse gas free hydrogen by thermocatalytic decomposition of methane–a review, Renew. Sustain. Energy Rev. 44 (2015) 221–256.

[12] M. Pudukudy, Z. Yaakob, Z.S. Akmal, Direct decomposition of methane over SBA-15 supported Ni, Co and Fe based bimetallic catalysts, Appl. Surf. Sci. 330 (2015) 418–430.

[13] J.D. Holladay, J. Hu, D.L. King, Y. Wang, An overview of hydrogen production technologies, Catal. Today 139 (2009) 244–260.

[14] D. Kang, J.W. Lee, Enhanced methane decomposition overnickel-carbon-B$_2$O$_3$ core-

shell catalysts derived from carbon dioxide, Appl. Catal. B 186 (2016) 41–55.

[15] M. Pudukudy, Z. Yaakob, Q. Jia, M.S. Takriff, Catalytic decomposition of undiluted methane into hydrogen and carbon nanotubes over Pt promoted Ni/CeO$_2$ catalysts, New J. Chem. 42 (2018) 14843–14856.

[16] H. Wang, R.T.K. Baker, Decomposition of methane over a Ni−Cu−MgO catalyst to produce hydrogen and carbon nanofibers, J. Phys. Chem. B 108 (2004) 20273–20277.

[17] K. Srilatha, D. Bhagawan, D. Srinivasulu, V. Himabindu, Comparison study between Ni/TiO$_2$ and Ni/flame synthesized TiO$_2$ catalysts for hydrogen production using thermocatalytic decomposition of methane, South Afr. J. Chem. Eng. 25 (2018) 91–97.

[18] A. Venugopal, S.N. Kumar, J. Ashok, D.H. Prasad, V.D. Kumari, K. Prasad, M. Subrahmanyam, Hydrogen production by catalytic decomposition of methane over Ni/SiO$_2$, Int. J. Hydrogen Energy 32 (2007) 1782–1788.

[19] S. Takenaka, Y. Shigeta, E. Tanabe, K. Otsuka, Methane decomposition into hydrogen and carbon nanofibers over supported Pd−Ni catalysts: characterization of the catalysts during the reaction, J. Phys. Chem. B 108 (2004) 7656–7664.

[20] R.K. Singh, A. Yadav, A. Agrawal, A. Shukla, Sh. Adak, T. Sasaki, R. Bal, Synthesis of highly coke resistant Ni nanoparticles supported MgO/ZnO catalyst for reforming of methane with carbon dioxide, Appl. Catal. B 191 (2016) 165–178.

[21] C. Shi, P. Zhang, Role of MgO over Al$_2$O$_3$-supported Pd catalysts for carbon dioxide reforming of methane, Appl. Catal. B 170–171 (2015) 43–52.

[22] Z. Boukha, C.J. González, M.G. Calvo, B. de Rivas, J.R.G. Velasco, J.I.G. Ortiz, R.L. Fonseca, MgO/NiAl$_2$O$_4$ as a new formulation of reforming catalysts: tuning the surface properties for the enhanced partial oxidation of methane, Appl. Catal. B 199 (2016) 372–383.

[23] S.D. Stefanidis, S.A. Karakoulia, K.G. Kalogiannis, E.F. Iliopoulou, A. Delimitis, H. Yiannoulakis, T. Zampetakis, A.A. Lappas, K.S. Triantafyllidis, Natural magnesium oxide (MgO) catalysts: a cost-effective sustainable alternative to acid zeolites for the in situ upgrading of biomass fast pyrolysis oil, Appl. Catal. B 196 (2016) 155–173.

[24] F. Bimbela, J. Ábrego, R. Puerta, L. García, J. Arauzo, Triantafyllidis, Catalytic steam reforming of the aqueous fraction of bio-oil using Ni-Ce/Mg-Al catalysts, Appl. Catal. B 15 (2017) 346–357.

[25] L. Xu, H. Song, L. Chou, Carbon dioxide reforming of methane over ordered mesoporous NiO-MgO-Al$_2$O$_3$ composite oxides, Appl. Catal. B 108–109 (2011) 177–190.

[26] A. Rastegarpanah, M. Rezaei, F. Meshkani, H.X. Dai, H. Arandiyan, Thermocatalytic decomposition of methane over mesoporous Ni/xMgO·Al$_2$O$_3$ nanocatalysts, Int. J. Hydrogen Energy 43 (2018) 15112–15123.

[27] N. Bayat, M. Rezaei, F. Meshkani, CO$_x$-free hydrogen and carbon nanofibers production by methane decomposition over nickel-alumina catalysts, Korean J. Chem. Eng. 33 (2016) 490–499.

[28] A. Rastegarpanah, F. Meshkani, M. Rezaei, Thermocatalytic decomposition of methane over mesoporous nanocrystalline promoted Ni/MgO·Al$_2$O$_3$ catalysts, Int. J. Hydrogen Energy 42 (2017) 16476–16488.

[29] A. Rategarpanah, F. Meshkani, Y. Wang, H. Arandiyan, M. Rezaei, Thermocatalytic conversion of methane to highly pure hydrogen over Ni–Cu/MgO·Al$_2$O$_3$ catalysts: influence of noble metals (Pt and Pd) on the catalytic activity and stability, Energy Convers. Manage. 168 (2018) 268–280.

[30] N. Bayat, M. Rezaei, F. Meshkani, Methane dissociation to CO$_x$-free hydrogen and carbon nanofiber over Ni-Cu/Al$_2$O$_3$ catalysts, Fuel 195 (2017) 88–96.

[31] N. Bayat, F. Meshkani, M. Rezaei, Thermocatalytic decomposition of methane to CO$_x$-free hydrogen and carbon over Ni–Fe–Cu/Al$_2$O$_3$ catalysts, Int. J. Hydrogen Energy 41 (2016) 13039–13049.

[32] S. Takenaka, Y. Shigeta, E. Tanabe, K. Otsuka, Methane decomposition into hydrogen and carbon nanofibers over supported Pd-Ni catalysts, J. Catal. 220 (2003) 468–477.

[33] H. Ogihara, S. Takenaka, I. Yamanaka, E. Tanabe, A. Genseki, K. Otsuka, Formation of highly concentrated hydrogen through methane decomposition over Pd-based alloy catalysts, J. Catal. 238 (2006) 353–360.

[34] M.J. Lázaro, Y. Echegoyen, I. Suelves, J.M. Palacios, R. Moliner, Decomposition of methane over Ni-SiO$_2$ and Ni-Cu-SiO$_2$ catalysts: effect of catalyst preparation method, Appl. Catal. A 329 (2007) 22–29.

[35] T.V. Reshetenko, L.B. Avdeeva, Z.R. Ismagilov, A.L. Chuvilin, V.A. Ushakov, Carbon capacious Ni-Cu-Al$_2$O$_3$ catalysts for high-temperature methane decomposition, Appl. Catal. A 247 (2003) 51–63.

[36] J. Chen, Y. Li, Z. Li, X. Zhang, Production of CO$_x$-free hydrogen and nanocarbon by direct decomposition of undiluted methane on Ni–Cu–alumina catalysts, Appl. Catal. A 269 (2004) 179–186.

[37] N. Bayat, M. Rezaei, F. Meshkani, Methane decomposition over Ni–Fe/Al$_2$O$_3$ catalysts for production of CO$_x$-free hydrogen and carbon nanofiber, Int. J. Hydrogen Energy 41 (2016) 1574–1584.

[38] S.M. Morris, P.F. Fulvio, M. Jaroniec, Ordered mesoporous alumina-supported metal oxides, J. Am. Chem. Soc. 130 (2008) 15210–15216.

[39] N. Popova, R.K. Salakhova, K. Dosumov, S. Tungatarova, A. Sass, Z. Zheksenbaeva, L. Komashko, V. Grigor'eva, A. Shapovalov, Nickel-copper-chromium catalyst for selective methane oxidation to synthesis gas at short residence times, Kinet. Catal. 50 (2009) 567–576.

[40] J. Dufour, C. Martos, A. Ruiz, F.J. Ayuela, Effect of the precursor on the activity of high temperature water gas shift catalysts, Int. J. Hydrogen Energy 38 (2013) 7647–7653.

[41] F. Meshkani, M. Rezaei, Preparation of nanocrystalline metal (Cr, Al, Mn, Ce, Ni, Co and Cu) modified ferrite catalysts for the high temperature water gas shift reaction,

[42] N. Lohitharn, J.G. Goodwin Jr, Impact of Cr, Mn and Zr addition on Fe Fischer Tropsch synthesis catalysis: Investigation at the active site level using SSITKA, J. Catal. 257 (2008) 142–151.

[43] L. Ni, K. Kuroda, L.-P. Zhou, T. Kizuka, K. Ohta, K. Matsuishi, J. Nakamura, Kinetic study of carbon nanotube synthesis over Mo/Co/MgO catalysts, Carbon 44 (2006) 2265–2272.

[44] A.E. Awadallah, A.A. Aboul-Enein, A.K. Aboul-Gheit, Impact of group VI metals addition to Co/MgO catalyst for non-oxidative decomposition of methane into COx-free hydrogen and carbon nanotubes, Fuel 129 (2014) 27–36.

[45] S. Chitsazan, S. Sepehri, G. Garbarino, M.M. Carnasciali, Steam reforming of biomass-derived organics: interactions of different mixture components on Ni/Al$_2$O$_3$ based catalysts, Appl. Catal. B 187 (2016) 386–398.

[46] A.E. Awadallah, Promoting effect of group VI metals on Ni/MgO for catalytic growth of carbon nanotubes by ethylene chemical vapour deposition, Chem. Pap. 69 (2015) 316–324.

[47] K. Jabbour, P. Massiani, A. Davidson, S. Casale, N. El Hassan, Ordered mesoporous "one-pot" synthesized Ni-Mg (Ca)-Al$_2$O$_3$ as effective and remarkably stable catalysts for combined steam and dry reforming of methane (CSDRM), Appl. Catal. B 201 (2017) 527–542.

[48] J.-G. Li, T. Ikegami, J.-H. Lee, T. Mori, Y. Yajima, A wet-chemical process yielding reactive magnesium aluminate spinel (MgAl$_2$O$_4$) powder, Ceram. Int. 127 (2001) 481–489.

[49] D. Dini, Y. Halpin, J.G. Vos, E.A. Gibson, The influence of the preparation method of NiO$_x$ photocathodes on the efficiency of p-type dye-sensitized solar cells, Coord. Chem. Rev. 304 (2015) 179–201.

[50] J. Li, C. Xiao, L. Xiong, X. Chen, L. Zhao, L. Dong, Y. Du, Y. Yang, H. Wang, S. Peng, Hydrogen production by methane decomposition over Ni-Cu-SiO$_2$ catalysts: effect of temperature on catalyst deactivation, RSC Adv. 6 (2016) 52154–52163.

[51] G.D. Nuernberg, E.L. Foletto, C.E. Campos, H.V. Fajardo, N.L. Carreño, L.F. Probst, Direct decomposition of methane over Ni catalyst supported in magnesium aluminate, J. Power Sources 208 (2012) 409–414.

[52] B.K. Choi, Y.H. Park, D.J. Moon, N.C. Park, Y.C. Kim, Effect of bimetallic Ni-Cr catalysts for steam-CO$_2$ reforming of methane at high pressure, J. Nanosci. Nanotechnol. 15 (2015) 5259–5263.

[53] L. Kaluža, D. Gulková, Z. Vit, M. Zdražil, Effect of support type on the magnitude of synergism and promotion in CoMo sulphide hydrodesulphurisation catalyst, Appl. Catal. A 324 (2007) 30–35.

[54] K.V. Chary, T. Bhaskar, G. Kishan, K.R. Reddy, Characterization and reactivity of molybdenum oxide catalysts supported on niobia, J. Phys. Chem. B 105 (2001) 4392–4399.

[55] M.N. Isaza, Z. Pachon, V. Kafarov, D.E. Resasco, Deactivation of Ni-Mo/Al$_2$O$_3$ catalysts aged in a commercial reactor during the hydrotreating of deasphalted vacuum residuum, Appl. Catal. A 199 (2000) 263–273.

[56] J. Sheng, X. Yi, F. Li, W. Fang, Effects of tungsten on the catalytic activity of Ni–W catalysts for the hydrogenation of aromatic hydrocarbons, React. Kinet. Mech. Catal. 99 (2010) 371–379.

[57] L. Yuan, X. Meng, S. Guo, Z. Li, H. Cui, L. Zhao, J. Wang, Comparison of oxide, sulfide, carbide and nitride Ni-W catalysts supported USY-Al$_2$O$_3$ for ring opening of decalin, Mol. Catal. 443 (2017) 253–261.

[58] Y. Liu, B. Liu, Q. Wang, C. Li, W. Hu, Y. Liu, P. Jing, W. Zhao, J. Zhang, Three-dimensionally ordered macroporous Au/CeO$_2$–Co$_3$O$_4$ catalysts with mesoporous walls for enhanced CO preferential oxidation in H$_2$-rich gases, J. Catal. 296 (2012) 65–76.

[59] Z. Li, G. Xu, G.B. Hoflund, In situ IR studies on the mechanism of methane oxidation over Pd/Al$_2$O$_3$ and Pd/Co$_3$O$_4$ catalysts, Fuel Process. Technol. 84 (2003) 1–11.

[60] Y.X. Liu, H.X. Dai, J.G. Deng, X.W. Li, Y. Wang, H. Arandiyan, S.H. Xie, H.G. Yang, G.S. Guo, Au/3DOM La$_{0.6}$Sr$_{0.4}$MnO$_3$: highly active nanocatalysts for the oxidation of carbon monoxide and toluene, J. Catal. 305 (2013) 146–153.

[61] H. Arandiyan, H.X. Dai, J.G. Deng, Y. Wang, H.Y. Sun, S.H. Xie, B.Y. Bai, Y.X. Liu, K.M. Ji, J.H. Li, Supported Ag nanoparticles for the combustion of methane, J. Phys. Chem C 118 (2014) 14913–14928.

[62] H.Y. Wang, A.C. Lua, Methane decomposition using Ni–Cu alloy nano-particle catalysts and catalyst deactivation studies, Chem. Eng. J. 262 (2015) 1077–1089.

[63] W. Ahmed, M.N. El-Din, A. Aboul-Enein, A. Awadallah, Effect of textural properties of alumina support on the catalytic performance of Ni/Al$_2$O$_3$ catalysts for hydrogen production via methane decomposition, J. Nat. Gas Sci. Eng. 25 (2015) 359–366.

[64] S.K. Saraswat, K. Pant, Ni–Cu–Zn/MCM-22 catalysts for simultaneous production of hydrogen and multiwall carbon nanotubes via thermo-catalytic decomposition of methane, Int. J. Hydrogen Energy 36 (2011) 13352–13360.

[65] G.D.B. Nuernberg, H.V. Fajardo, E.L. Foletto, S.M. Hickel-Probst, N.L. Carreño, L.F. Probst, J. Barrault, Methane conversion to hydrogen and nanotubes on Pt/Ni catalysts supported over spinel MgAl$_2$O$_4$, Catal. Today 176 (2011) 465–469.

[66] W. Fang, S. Paul, M. Capron, F. Dumeignil, L. Jalowiecki-Duhamel, Hydrogen production from bioethanol catalyzed by Ni$_X$Mg$_2$AlO$_Y$ ex-hydrotalcite catalysts, Appl. Catal. B 152 (2014) 370–382.

[67] L. Dong, Y. Du, J. Li, H. Wang, Y. Yang, S. Li, Z. Tan, The effect of CH$_4$ decomposition temperature on the property of deposited carbon over Ni/SiO$_2$ catalyst, Int. J. Hydrogen Energy 40 (2015) 9670–9676.

[68] M. Pudukudy, Z. Yaakob, M.Z. Mazuki, M.S. Takriff, S.S. Jahaya, One-pot sol-gel synthesis of MgO nanoparticles supported nickel and iron catalysts for undiluted methane decomposition into CO$_x$ free hydrogen and nanocarbon, Appl. Catal. B 218 (2017) 298–316.